Dynamics of fluctuations in smectic membranes

Irakli Sikharulidze and Wim H. de Jeu
FOM-Institute for Atomic and Molecular Physics, Kruislaan 407, 1098 SJ Amsterdam, The Netherlands
(Received 15 December 2004; published 15 July 2005)

We present a comprehensive account of the dynamics of layer-displacement fluctuations in smectic liquid-crystal membranes as studied by x-ray photon correlation spectroscopy (XPCS) and neutron-spin echo (NSE). Combining these two techniques at fast relaxation times, three distinct relaxation regimes can be distinguished. For thin membranes, at the specular Bragg position oscillatory relaxation occurs, which transforms for thicker samples into exponential decay. Above a critical off-specular angle, in XPCS exponential relaxation is observed that does not depend on the scattering angle. This indicates relaxation times that are independent of the wavelength of the fluctuations. In this regime the relaxation of the fluctuations is dominated by the surface tension. Using NSE larger off-specular angles can be reached than by XPCS, for which the relaxation time decreases with the scattering angle. This regime is dominated by the bulk elasticity of the smectic membrane. The results are compared with theoretical models for the fluctuation behavior of smectic membranes, in which effects of the mosaic distribution and of the center of mass movement of the smectic membranes must be incorporated.

DOI: 10.1103/PhysRevE.72.011704 PACS number(s): 61.30.−v, 61.10.Kw, 42.25.Kb

I. INTRODUCTION

In a three-dimensional (3D) crystal the particles vibrate around well-defined lattice positions with an amplitude small compared to the lattice spacing. As the dimensionality of the system is decreased, fluctuations become increasingly important. As a result long-range translational order cannot exist in 2D and 1D; it would be destroyed by thermal fluctuations. The spatial dimension at which thermal fluctuations just prevent the existence of long-range order is called the lower marginal dimensionality, which for solids has the value 2. In this case, the positional correlations decay algebraically as a function of distance. Low-dimensional ordering and the associated fluctuation behavior are of considerable interest and can also be observed in 3D systems that are ordered in one direction only. This situation has been studied for a wide variety of systems comprising smectic liquid crystal films, Langmuir films, Newtonian black films, and surfactant and lipid membranes [1]. Smectic liquid crystals are often used as model systems of specific types of ordering as they provide a variety of different phases and phase transitions. The simplest type of smectic phase is smectic-*A* (Sm*A*), in which the elongated molecules are organized in stacks of liquid layers. In addition the long molecular axes are, on average, parallel to the layer normal. Hence a periodic structure exists in one dimension: the rodlike molecules form a density wave along the layer normal, while the system remains fluid in the other two directions.

Sm*A* liquid crystals are an example of a 3D system at its lower marginal dimensionality. The correlation function describing the periodicity of the smectic layers decays algebraically as $r^{-\eta}$, in which the exponent η is small and positive. In x-ray scattering, instead of δ-function-type Bragg peaks with diffuse tails characteristic of 3D crystal periodicity, power-law singularities corresponding to the smectic layering have been observed [2–4]. The thermal fluctuation modes in smectics correspond to bending and compression of the layers, characterized by elastic constants K and B, respectively. Defining $u(\mathbf{r})$ as the layer displacement from its equilibrium position, $\langle u^2(\mathbf{r})\rangle$ is found to diverge logarithmically with the sample size (Landau-Peierls instability) [5]:

$$\langle u^2(\mathbf{r})\rangle = \frac{k_B T}{8\pi\sqrt{KB}} \ln\left(\frac{L}{d}\right). \tag{1}$$

Here L is the thickness of the system, d the smectic layer periodicity, and $k_B T$ the thermal energy. At large sample size the long-range order is destroyed by the thermal fluctuations of the system even though the algebraic decay is slow.

A unique property of smectic liquid crystals is their ability to form films that are freely suspended or free standing over an aperture in a frame. This property has been known since the beginning of the last century. Friedel [6] used it in his monograph on liquid crystals as an argument in favor of the existence of layers in the smectic phase. However, it was not before the 1970s that such films found extensive usage in experimental studies [7–9]. The smectic layers align parallel to the two air-film surfaces, which are flat because the surface tension minimizes the surface area of the film. Apart from the edges, such films are substrate free and can be considered as membranes consisting of stacks of smectic layers. They have a high degree of uniformity: the alignment of the smectic layers is almost perfect, allowing one to study single-domain samples of various thickness. The surface area can be as large as 1000 mm^2, while the thickness can be easily varied from thousands of layers (tens of μm) down to two layers (about 5 nm). The average effects of the fluctuations in smectic membranes have been extensively investigated by static x-ray scattering [10,11]. An important result is that under most practical circumstances the fluctuations of the smectic layers are conformal: they are uniform across the film. Evidently, a loss of conformality is expected for very thick membranes. In thin membranes it has been observed in

off-specular (diffuse) x-ray reflectivity for fluctuations with a small in-plane wavelength below about 30–50 nm.

If coherent light is incident on a material, the scattered intensity shows a so-called speckle pattern that reflects the instantaneous configuration of the scatterers. Movement of the scatterers causes a corresponding change in this pattern and thus contains information on the dynamics of the system. Photon correlation spectroscopy (PCS) or dynamic light scattering measures the time-dependent intensity autocorrelation function of the speckle pattern. Using visible light it has become a well-established technique since lasers became available [12]. In contrast, correlation spectroscopy with coherent x rays has only been developed during the last decade at third-generation high-brilliance synchrotron sources [13–15]. Dynamic light-scattering studies of smectic membranes were carried out by Böttger and Joosten [16] and Nallet, Roux, and Prost [17] and more recently x-ray photon correlation spectroscopy (XPCS) has been successfully applied to the measurement of liquid crystal and polymer dynamics [18–21]. First experiments probing the dynamics of the fluctuations in smectic membranes using XPCS were carried out by Price *et al.* [22] using soft x rays, and by de Jeu and co-workers using conventional x rays [23–25]. Extensive theoretical models of fluctuations in smectic membranes have been developed in recent years [26–36]. Note that light-scattering experiments are sensitive either to orientational fluctuations of the director associated with the layer undulations [27,37] or to long-wavelength fluctuations of the air-liquid interface (as in the case of Ref. [16]). In contrast, XPCS is sensitive to the layer fluctuations and provides in addition a much better spatial resolution. Both for light scattering and x-ray scattering of smectic membranes, finite-size and surface effects, depending on the surface tension and perhaps other surface parameters, should be taken into account. Most importantly, the finite thickness of a smectic membrane leads to quantization, producing a set of modes dependent on surface parameters, instead of a continuous fluctuation spectrum as in bulk systems.

During the last years we have extended XPCS into the nanosecond range [24], which also opened the possibility of combining this technique with neutron spin-echo (NSE) methods [25]. As a follow-up of the results in these Letters, we present is this paper a detailed account of the dynamics of fluctuations in smectic membranes. The next section summarizes the theory, adapted to the discussion of the experimental results in the subsequent sections. In Sec. III we discuss the experimental aspects including the influence of the x-ray beam on the sample stability. A full technical discussion of the effects of coherence and resolution in XPCS of smectic membranes has been given elsewhere [38]. The results given in Sec. IV include a transition from oscillatory relaxation of the fluctuations (due to inertial effects) to simple exponential relaxation of overdamped fluctuations, as a function both of membrane thickness and of the off-specular angle. In the exponential regime the damping is dominated by the surface tension. Finally, at smaller length scales of the fluctuations bulk elasticity is expected to become increasingly important. The transition to this regime has been observed by combining fast XPCS with NSE. The results are discussed in Sec. V with emphasis on the factors that influence the determining wavelength from the fluctuation spectrum and on the problems associated with the choice of this quantity in the limit $q_\perp \to 0$.

II. THEORY

A. X-ray scattering

In x-ray scattering the amplitude of the scattered field $E(\mathbf{q})$ is related to the Fourier transform of the electron density distribution within the sample $\rho(\mathbf{r})$. The intensity of the scattered x rays $I(\mathbf{q})=\langle E(\mathbf{q})E^*(\mathbf{q})\rangle$ is proportional to the structure factor $S(\mathbf{q})$:

$$S(\mathbf{q}) = \int\int d^3\mathbf{r}_1 d^3\mathbf{r}_2 \rho(\mathbf{r}_1)\rho(\mathbf{r}_2)\exp[-i\mathbf{q}\cdot(\mathbf{r}_1-\mathbf{r}_2)], \quad (2)$$

in which $\mathbf{q}=(\mathbf{q}_\perp, q_z)$ represents the scattering vector and $\mathbf{r}_1$ and $\mathbf{r}_2$ define positions within the scattering volume. If $\rho(\mathbf{r})$ changes in time, $S(\mathbf{q})$ also becomes time dependent and is usually referred to as the intermediate scattering function.

In a cylindrical coordinate system $\mathbf{r}=(\mathbf{r}_\perp, z)=(x,y,z)$ with the z axis perpendicular to the surface of the smectic membrane, the density profile of this stack of liquid layers at position $z-nd$ can be represented as [26]:

$$\rho(\mathbf{r}_\perp, z, t) = \rho_{layer}(z) * \sum_{n=0}^{N} \delta(z - nd - u_n(\mathbf{r}_\perp, t)), \quad (3)$$

where n indicates a specific smectic layer, N the total number of layers, $u_n(\mathbf{r}_\perp, t)$ the displacement of the nth smectic layer from its equilibrium position, and $\rho_{layer}(z)$ the density profile of a single smectic layer. This equation reflects that a smectic membrane is homogeneous in the (x,y) plane, while it has an inhomogeneous, layered structure in the z direction.

B. Intensity-intensity time correlation function

In this section we summarize the calculation of the intensity-intensity time correlator $\langle I(t)I(0)\rangle$ that is measured in XPCS experiments, defined as

$$\langle I(t)I(0)\rangle = \frac{1}{T}\int_0^T d\tau E(\tau)E^*(\tau)E(t+\tau)E^*(t+\tau). \quad (4)$$

According to Eq. (2) the intensity correlator can be rewritten in the form

$$\langle I(t)I(0)\rangle = \int\int\int\int d\mathbf{r}_1 d\mathbf{r}_2 d\mathbf{r}_3 d\mathbf{r}_4 e^{-i\mathbf{q}\cdot(\mathbf{r}_1-\mathbf{r}_2)-i\mathbf{q}\cdot(\mathbf{r}_3-\mathbf{r}_4)} \times\langle\rho(\mathbf{r}_1,0)\rho(\mathbf{r}_2,0)\rho(\mathbf{r}_3,t)\rho(\mathbf{r}_4,t)\rangle. \quad (5)$$

The integration is performed over the coherence volume, the size of which can differ from the scattering volume. In XPCS the two sizes should preferably match. In the further discussion we will assume that this is the case and use coherence and scattering volume as synonyms.

The density of a membrane can be split into two parts: $\rho(\mathbf{r}_\perp, z, t)=\rho_0(z,t)+\Delta\rho(\mathbf{r}_\perp, z, t)$. The first term $\rho_0(z,t)$ represents the average displacement of a layer within the scatter-

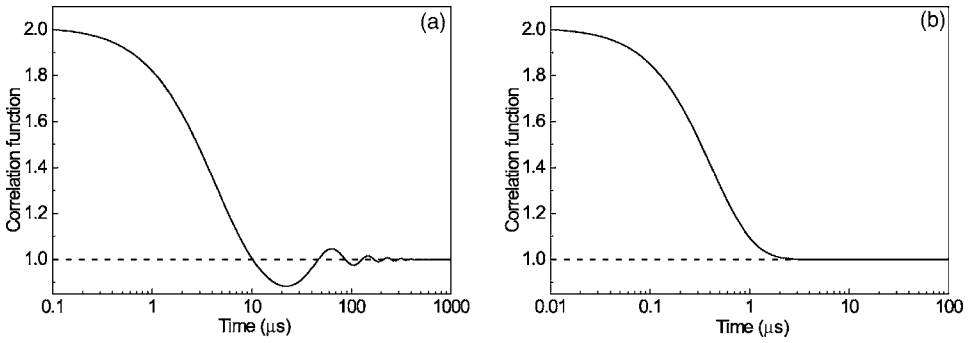

FIG. 1. Intensity correlation functions calculated for a 2-μm membrane: (a) hetorodyne case and (b) homodyne case. The graphs are renormalized for clarity.

ing volume in the z direction at time t, while $\Delta\rho(\mathbf{r}_\perp,z,t)$ denotes time-dependent fluctuations. We assume that the membranes are incompressible and that all the layers are undulating conformally ("unisono"). In this case $\rho_0(z,t)$ contains only translations of the scattering volume that do not change the scattered intensity, and we can drop the index n in the layer displacement function $u_n(\mathbf{r}_\perp,t)$. Then the total scattered field can be split in two parts:

$$E(\tau) = E_0(t) + \delta E(t), \tag{6}$$

where $E_0(t)$ and $\delta E(t)$ correspond to $\rho_0(z,t)$ and $\Delta\rho(\mathbf{r}_\perp,z,t)$, respectively. In this situation we can consider $E_0(t)$ as a constant "reference" signal. The normalized correlation functions of the fluctuating electric field are defined as

$$g_1(t) = \frac{\langle \delta E(\tau)\,\delta E^*(\tau+t)\rangle}{\langle I_s\rangle}, \tag{7}$$

$$g_2(t) = \frac{\langle \delta E(\tau)\,\delta E^*(\tau)\,\delta E(\tau+t)\,\delta E^*(\tau+t)\rangle}{\langle I_s\rangle^2}, \tag{8}$$

where $I_0=\langle E_0E_0^*\rangle$ and $I_s=\langle \delta E(t)\,\delta E^*(t)\rangle$. Using these definitions and Eq. (6), the intensity correlator in Eq. (4) can be expressed in the form [39]

$$\langle I(t)I(0)\rangle = (I_0+I_s)^2 + 2I_0I_s\,\mathrm{Re}[g_1(t)] + I_s^2(g_2(t)-1). \tag{9}$$

This formalism allows us to distinguish in XPCS two different detection schemes: heterodyne and homodyne. The heterodyne regime is characterized by $\delta E(t) \ll E_0$, for which situation the weak scattered intensity I_s is amplified by the strong reference signal I_0. Consequently, the last term in Eq. (9) can be omitted and the correlator is determined by $g_1(t)$. Homodyne detection applies to the situation that the reference signal I_0 is absent. Then the right-hand side in Eq. (9) equals $I_s^2g_2(t)$. By definition I_0 reflects translations of the scattering volume and thus contributes a δ-function-like signal at the specular position. Depending on the scattering geometry we either catch this reflection or not. In this way the presence of the reference signal I_0 can be controlled and the measurement switches between homodyne and heterodyne detection.

Both $g_1(t)$ and $g_2(t)$ can be expressed in terms of the density correlations in the membrane. The correlator $g_1(t)$ is proportional to the intermediate scattering function

$$\langle \delta E(\tau)\,\delta E^*(\tau+t)\rangle \sim S(\mathbf{q},t) = \int d\mathbf{r}_1 d\mathbf{r}_2 e^{-i\mathbf{q}\cdot(\mathbf{r}_1-\mathbf{r}_2)} \times\langle \Delta\rho(\mathbf{r}_1,\tau)\Delta\rho(\mathbf{r}_2,\tau+t)\rangle. \tag{10}$$

If we assume the density fluctuations $\Delta\rho(\mathbf{r},t)$ to be Gaussian, we can express $g_2(t)$ as a function of $g_1(t)$. Using Wick's theorem to factor out the four-point density correlator in Eq. (5) [40], we obtain

$$\begin{aligned}\langle \Delta\rho(\mathbf{r}_1,0)\Delta\rho(\mathbf{r}_2,0)\Delta\rho(\mathbf{r}_3,t)\Delta\rho(\mathbf{r}_4,t)\rangle &= \langle \Delta\rho(\mathbf{r}_1,0)\Delta\rho(\mathbf{r}_2,0)\rangle\langle \Delta\rho(\mathbf{r}_3,t)\Delta\rho(\mathbf{r}_4,t)\rangle \\ &+ \langle \Delta\rho(\mathbf{r}_1,0)\Delta\rho(\mathbf{r}_3,t)\rangle\langle \Delta\rho(\mathbf{r}_2,0)\Delta\rho(\mathbf{r}_4,t)\rangle \\ &+ \langle \Delta\rho(\mathbf{r}_1,0)\Delta\rho(\mathbf{r}_4,t)\rangle\langle \Delta\rho(\mathbf{r}_2,0)\Delta\rho(\mathbf{r}_3,t)\rangle.\end{aligned} \tag{11}$$

Introducing this expansion into Eq. (5), $g_2(t)$ can be written as a sum of three terms: $g_2(t)=I_1+I_2+I_3$, each of which is the Fourier transform of the corresponding term in Eq. (11). In I_1 the two positions in the correlators are taken at the same time. Consequently, after time averaging they become time independent and I_1 results in the average intensity squared. In the case of an infinite scattering volume the integration in Eq. (5) is extended until infinity and the correlator $\langle \rho(\mathbf{r}_1,0)\rho(\mathbf{r}_3,t)\rangle$ in I_2 depends only on the vector difference $\mathbf{r}_1-\mathbf{r}_3$. As a consequence this term contributes in Eq. (11) to the scattering at a zero angle only and is usually omitted. The remaining term I_3 is equal to the squared modulus of $g_1(t)$. As a result Eq. (5) transforms into the following equation, known as the Siegert relation:

$$g_2(t) = 1 + |g_1(t)|^2. \tag{12}$$

Note that the validity of this relation depends critically on the neglect of the term I_2. The consequences of inclusion of I_2 are considered in Appendix A.

Figure 1(a) shows a correlation function in the heterodyne detection scheme. According to Eq. (9), in this case $g_1(t)$ defines the profile of the measured intensity correlation function. Such oscillating profiles have been frequently observed in XPCS measurements at specular positions where the reference intensity I_0 is present [24]. In contrast, at off-specular positions this signal is absent. XPCS measurements in this homodyne regime indicate a simple exponential relaxation of the intensity correlation function that can be fitted using the Siegert relation [24].

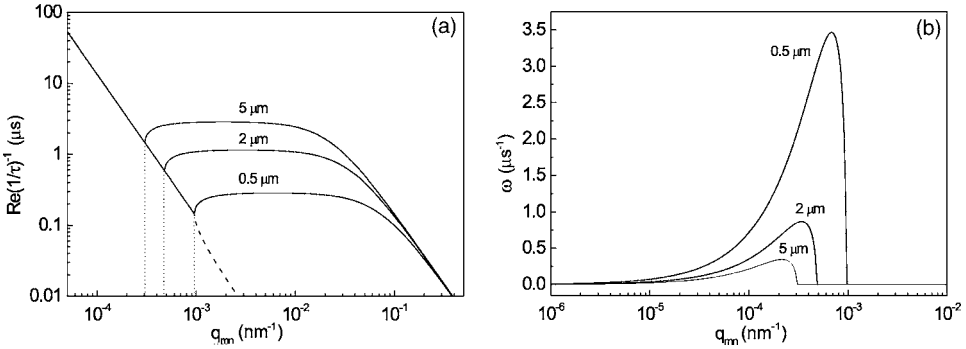

FIG. 2. Dispersion curves for the relaxation of fluctuations of 8CB smectic membranes for three different thicknesses calculated according to Eqs. (21) and (22) using the parameters from Table I. (a) Dependence of the relaxation time on the wave vector q_{mn}. The dotted lines indicate for each thickness the transition wave vector q_c; the dashed line give the fast relaxation branch for 0.5 μm. (b) Dependence of the frequency of the fluctuations on the wave vector q_{mn}.

C. Relaxation regimes

Using the smectic membrane density profile given in Eq. (3) we can express $S(q,t)$ in the following form:

$$S(\mathbf{q},t) = |\tilde{\rho}_{layer}(q_z)|^2 \int d\mathbf{r}_{1,\perp} d\mathbf{r}_{2,\perp} e^{-i\mathbf{q}_\perp \cdot (\mathbf{r}_{1,\perp} - \mathbf{r}_{2,\perp})} \times \sum_{m,n} \exp[i(m-n)dq_z - q_z^2\langle u^2\rangle - q_z^2 G(\mathbf{r}_{\perp,1} - \mathbf{r}_{\perp,2}, t)]. \tag{13}$$

Here $\tilde{\rho}_{layer}(q_z)$ is the Fourier image of the smectic layer density profile $\rho_{layer}(z)$. The layer displacement correlation function $G(\mathbf{r}_{\perp,1} - \mathbf{r}_{\perp,2}, t) = \langle (u(\mathbf{r}_{1,\perp},0) - u(\mathbf{r}_{2,\perp},t))^2 \rangle$ can be expressed for a rectangular membrane of dimensions (L_x, L_y) and thickness L in the following form (see Appendix B):

$$G(\mathbf{r}_{\perp,1} - \mathbf{r}_{\perp,2}, t) = 2k_B T \sum_{m,n=1}^{\infty} \frac{1}{KLq_{mn}^4 + 2\gamma q_{mn}^2} \times \cos\left(\frac{\pi m}{L_x}(x_1 - x_2)\right) \times \cos\left(\frac{\pi n}{L_y}(y_1 - y_2)\right) \times \frac{\tau_1 \exp\left(-\frac{t}{\tau_1}\right) - \tau_2 \exp\left(-\frac{t}{\tau_2}\right)}{\tau_1 - \tau_2}. \tag{14}$$

In this expression γ represents the surface tension and q_{mn} the wave vector of a specific fluctuation defined as

$$q_{mn}^2 = \left(\frac{\pi m}{L_x}\right)^2 + \left(\frac{\pi n}{L_y}\right)^2. \tag{15}$$

According to Eq. (B35) of Appendix B the relaxation times τ_1 and τ_2 can be written as

$$\frac{1}{\tau_{1,2}} = \frac{\eta_3 q_{mn}^2}{2\rho_0}\left[1 \mp i\sqrt{\frac{4\rho_0}{\eta_3^2 q_{mn}^4}\left(Kq_{mn}^4 + \frac{2\gamma}{L}q_{mn}^2\right) - 1}\right] = a(q_{mn}) \mp if(q_{mn}), \tag{16}$$

where

$$a(q_{mn}) = \frac{\eta_3 q_{mn}^2}{2\rho_0}, \tag{17}$$

$$f(q_{mn}) = \frac{\eta_3 q_{mn}^2}{2\rho_0}\sqrt{\frac{4\rho_0}{\eta_3^2 q_{mn}^4}\left(Kq_{mn}^4 + \frac{2\gamma}{L}q_{mn}^2\right) - 1}. \tag{18}$$

Figure 2(a) shows the dependence of the real part of the relaxation times τ_1 and τ_2 on the wave vector of a particular fluctuation. The nature of the dispersion curve changes at a crossover wave vector q_c for which the square root in Eq. (18) changes sign. For the small values q_{mn} involved we can disregard the term in q_{mn}^4. Then the relaxation times τ_1 and τ_2 can be represented in the form

$$\tau_{1,2} \approx \frac{2\rho_0}{\eta_3 q_{mn}^2}\left(1 \mp i\sqrt{\frac{8\rho_0\gamma}{\eta_3^2 L q_{mn}^2} - 1}\right)^{-1}. \tag{19}$$

The crossover then is given by

$$q_c \approx \sqrt{\frac{8\rho_0\gamma}{\eta_3^2 L}}. \tag{20}$$

In the region $q_{mn} < q_c$ the function $f(q_{mn})$ is real and the relaxation times τ_1 and τ_2 are complex conjugate numbers. This regime corresponds to a combination of exponential relaxation and oscillatory behavior. From Eqs. (17) and (18) we derive the following expressions for the relaxation time τ and the frequency ω

$$\tau(q_{mn}) = \frac{2\rho_0}{\eta_3 q_{mn}^2}, \tag{21}$$

$$\omega(q_{mn}) = \frac{\eta_3 q_{mn}^2}{2\rho_0}\sqrt{\frac{4\rho_0}{\eta_3^2 q_{mn}^4}\left(Kq_{mn}^4 + \frac{2\gamma}{L}q_{mn}^2\right) - 1}. \quad (22)$$

Note that the relaxation time does not depend on the membrane thickness while the frequency decreases with thickness as $1/\sqrt{L}$. The behavior of $\tau(q_{mn})$ and $\omega(q_{mn})$ according to Eqs. (21) and (22) is illustrated in Fig. 2 for three membranes of different thicknesses.

In the region $q_{mn} > q_c$ both solutions are real. Figure 2 shows that τ_2 strongly decreases with increasing wave vector q_{mn}. The contribution of this fast relaxation to the correlation function is weighted by the value of τ_2 [see Eq. (14)] and consequently also decreases strongly with wave vector. Hence we can neglect this branch and consider for $q_{mn} > q_c$ only the slow branch with relaxation time τ_1. In this regime the elastic term Kq_{mn}^4 cannot be disregarded anymore. Using $8\rho_0\gamma/(\eta_3^2 L q_{mn}^2) \ll 1$, for large q_{mn} the square root can be expanded and we can write τ_1 in the simplified form:

$$\tau_1 = \frac{\eta_3}{2\gamma/L + Kq_{mn}^2}. \quad (23)$$

According to this equation we can divide the region $q_{mn} > q_c$ into two different subregimes. For $Kq_{mn}^2 < 2\gamma/L$ the second term in the denominator can be omitted and we arrive at

$$\tau_1 = \eta_3 L/(2\gamma). \quad (24)$$

In this "surface relaxation regime" the relaxation time depends only on the surface tension, the membrane thickness, and the viscosity. For $Kq_{mn}^2 > 2\gamma/L$ the second term in the denominator of Eq. (23) dominates and

$$\tau_1 = \eta_3/(Kq_{mn}^2). \quad (25)$$

This is the "bulk-elasticity relaxation regime" for which the relaxation time depends on the bending elasticity and the viscosity, and it is neither sensitive to the surface tension nor to the membrane thickness anymore.

III. EXPERIMENTAL

A. Smectic membrane samples

We studied the smectic liquid crystalline compounds N-(4-*n*-butoxybenzilidene)-4-*n*-octylaniline (4O.8), 4-heptyl-2-[4-(2-perfluorhexylethyl)phenyl]-pyrimidin (FPP) and 4-octyl-4′-cyanobiphenyl (abbreviated as 8CB). Their molecular structure and phase transitions are given in Fig. 3. In Table I summarizes values of relevant material parameters and the smectic periodicity of these compounds. The first compound 4O.8 is typical for a large class of standard liquid crystalline materials. The other ones have some special characteristics giving differences in material parameters. The fluorinated part of FPP is surface active (low surface tension) and relatively rigid (large layer compressibility *B*). 8CB has a strongly polar end group leading to "dimer" formation and a layer periodicity corresponding to partially overlapping molecules. It has also been chosen because of the convenience of a smectic-*A* phase at room temperature.

Smectic membranes were spread manually by wetting the edges of an opening in a metal holder by the mesogenic

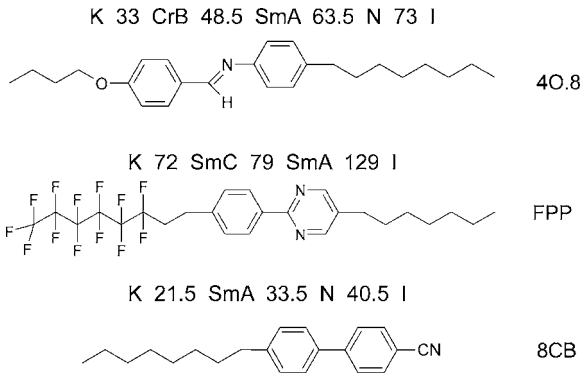

FIG. 3. The compounds: 4O.8 [23], FPP [10], and 8CB with their phase transition temperatures in °C. I stands for the isotropic phase, N for nematic, Sm*A* and Sm*C* for smectic-*A* and smectic-*C*, respectively, and CrB for crystalline B and K for crystal phases. The experiments were done in this order around 50, 100, and 27 °C, respectively.

compound in the smectic phase and then moving a spreader across the hole. By varying the amount of smectic material, the temperature, and the speed of drawing, relatively thin membranes ranging from 5 nm (two layers) to about 200 nm were produced. For x-ray reflectivity studies a large footprint of the incident x-ray beam must be accommodated. The membranes typically spanned a 10×25 mm^2 rectangular hole in a polished plate with sharp top edges. The sharp blades forced the membrane close to the top of the holder, reducing shadowing of the beam. Alternatively, a rectangular stainless-steel frame with sharp edges with a variable area was employed, in which two blades could be moved by a micrometer screw. Starting with smectic material at (almost) closed blades, thick membranes up to tens of μm were stretched to about 15×5 mm^2.

Directly after preparation, a film usually consists of regions of different thickness, from which it equilibrates to a uniform situation. The equilibration time varies from minutes to days depending on the specific compound, the temperature, and the type of frame. Usually the thinnest region grows at the expense of the thicker ones. The two surfaces of a membrane induce an almost perfect alignment of the smectic layers: the residual curvature of the film is mainly due to the nonplanarity of the edges of the holder. The resulting mosaic distribution, expressed as the angular spread of the surface normal, can be $\lesssim 0.001°$ over an area of about 100×500 μm^2 (footprint at high resolution) [38]. The membrane thickness can be easily determined by optical reflec-

TABLE I. Material parameters of the compounds investigated.

Parameter	4O.8	FPP	8CB
K (10^{-12} N)	5	10	20
B (10^7 N/m^2)	0.10	75	1.8
γ (10^{-3} N/m)	21	13	25
η_3 (kg m^{-1} s^{-1})	0.05	0.015	0.1
d (nm)	2.85	2.94	3.14

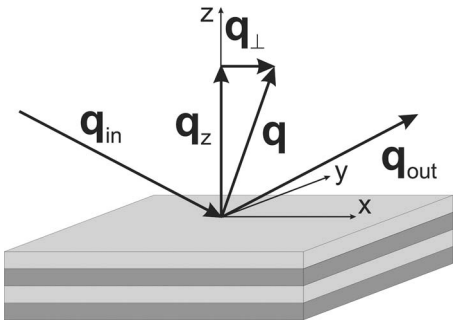

FIG. 4. Scattering geometry. $\mathbf{q}_{\text{in}}$ and $\mathbf{q}_{\text{out}}$ represent the incident and scattered wave vectors, respectively, and $\mathbf{q}$ is the scattering vector. $q_\perp$ and q_z are the projections of $\mathbf{q}$ on the surface and on the normal to the surface of the smectic membrane, respectively.

tivity, which for sufficiently thin films scales as the thickness squared [41,42]. The number of smectic layers in a film can be precisely determined from specular x-ray reflectivity. Reflection occurs both at the front and back interfaces, leading to constructive or destructive interference in dependence of the incoming angle (Kiessig or interference fringes). The period of the fringes is inversely proportional to the film thickness L. In addition, the internal periodic structure generates finite-size Bragg-like peaks centered at $q_n = 2\pi n/d$. Thus the number of smectic layers $N = L/d$ can be determined unambiguously. The smectic membranes are stable over many days or even months despite the fact that they are homogeneously compressed over their surface [42]. All measurements were done at the low-temperature region of the SmA range as indicated in Fig. 3.

B. X-ray scattering setup

Coherent x-ray scattering experiments were performed at the undulator beamline ID10A (Troika I) of the European Synchrotron Radiation Facility (ESRF, Grenoble). Membranes were usually mounted vertically in a reflection geometry (see Fig. 4). The incident wave vector $\mathbf{q}_{in}$ and the scattered wave vector $\mathbf{q}_{out}$ determine the wave vector transfer $\mathbf{q} = \mathbf{q}_{\text{out}} - \mathbf{q}_{\text{in}}$ with its modulus given by $q = (2\pi/\lambda)\sin\theta$, λ being the x-ray wavelength and 2θ the scattering angle. The membranes were illuminated either by 8 keV radiation ($\lambda = 0.155$ nm) or (to minimize absorption) by 13.4 keV radiation ($\lambda = 0.093$ nm). The energy was selected by a Si(111) monochromator followed by a Si mirror to suppress higher harmonics. The bandpass of the monochromator, given by $\Delta\lambda/\lambda \approx 10^{-4}$, determined the longitudinal coherence length of about 1.5 μm. The path length of the beam in the smectic membrane is given by $2L\sin\theta$ and should not exceed this value. This means that at the quasi-Bragg position corresponding to the smectic-layer spacing ($\theta \simeq 1.5°$), the membrane thickness should be restricted to $L \lesssim 30$ μm. The beam emerging from three undulators in series was collimated by a system of two slits and focused in the vertical direction by a refractive beryllium lens with a demagnification ratio of $\sim 1:1$. This symmetrized the transversal coherence lengths to about 10 μm, the same size as the 10-μm pinhole in front of the sample. Guard slits were placed after the pinhole to remove parasitic scattering. Using a 10-μm pinhole, at the Bragg angle the footprint of the beam was about 0.01×0.5 mm^2. At this position, the resulting mosaic distribution typically varied from 1 to 10 mdeg.

A fast avalanche photodiode (Perkin Elmer C30703) [43] with an intrinsic time resolution $\lesssim 2$ ns was used as detector at a distance of 1.5 m from the sample, with predetector slits typically set to 30×30 μm^2. The resolution of the setup was estimated to be $\Delta q_x \approx 10^{-4}$ nm^{-1} and $\Delta q_y = \Delta q_z \approx 10^{-3}$ nm^{-1}. Measurements were performed in the uniform filling mode of the storage ring consisting of 992 bunches at intervals of 2.8 ns.

The coherent photon flux at the sample for a 10-μm pinhole was about 1×10^9 counts s^{-1}/100 mA at 8 keV and about 5×10^7 counts s^{-1}/100 mA at 13.4 keV. The scattered intensity $I(t)$ was fed into a hardware autocorrelator that computed the normalized intensity-intensity time autocorrelation function $g_2(\tau)$. This was done in real time using a hardware multiple-tau digital autocorrelator FLEX01-8D (correlator.com, sampling time down to 8 ns). Ultimately the time structure of the storage ring limits the fastest accessible dynamics. Thanks to the perfect match between the millidegree mosaic distribution of the membranes and the high resolution of the setup, for thick samples at the Bragg position count rates up to tens of MHz were reached. This allowed measurements as a function of the wavelength of the fluctuations at off-specular positions ($q_\perp \neq 0$). However, the steep decrease of the intensity with $q_\perp$ still prevented access to fluctuations of wavelengths less than a few hundred nanometers. As we shall see, this limitation could be lifted using NSE.

C. Beam absorption and sample stability

The high brilliance of the x-ray beam at third-generation synchrotrons can have a destructive effect on many samples, in particular in the case of soft matter. For soft films on a substrate the x-ray beam probably generates free electrons in the substrate; these in turn migrate to the soft film and have a devastating ionizing effect. In the absence of a substrate, smectic membranes show a remarkable resistance to high-energy loads. The problems we encountered were not so much associated with irreversible beam damage but rather with heat absorption. Though in the case of XPCS the pinhole collimation reduces the total intensity strongly, the local flux does not change ($>10^{13}$ photons s^{-1} mm^{-2} @ Si(111), 8 keV). Hence even the high-resolution setup used in XPCS experiments puts exceptional stability requirements on the sample.

The heat generated by 8-keV x rays in a smectic membrane can be estimated as follows. At the Bragg angle $\theta \simeq 1.5°$ the path length for a membrane of thickness $L = 1.7$ μm is given by $L/\sin\theta \simeq 65$ μm. The absorption of hydrocarbons over this length is about 2% of the incident intensity of 10^9 photons/s, which amounts to 2×10^7 photons/s. At 8 keV this is equivalent to about 3×10^{-8} W. The width W of the beam and the height H perpendicular to the scattering plane are of the order of 10 μm, the size of the pinhole. Hence the absorption takes

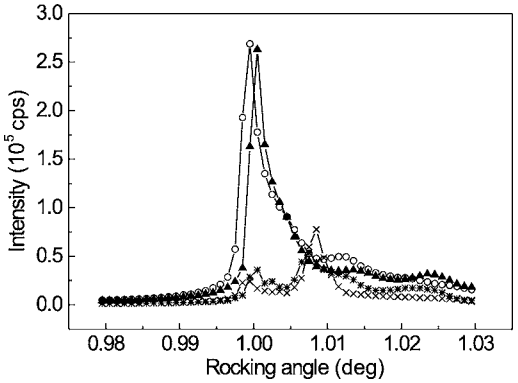

FIG. 5. Effects of beam absorbtion on the rocking curve of a 1.7-μm FPP membrane (10-μm pinhole). Circles: initial rocking curve. Crosses: after removal of one attenuator (3× increased intensity). Asterisks: immediately after inserting the attenuator again. Triangles: after equilibrating for 6 minutes.

place in a volume $V=(L/\sin\theta)WH\simeq 6\times 10^{-6}$ mm^3. For a density $\rho=10^3$ kg/m^3 and a specific heat of 2×10^3 J/(kg °C), this leads to an increase of the initial temperature in the illuminated volume of the order of 3 °C/s. At 13.4 keV the absorption is a factor of 4 less. The absorption volume is imbedded in the membrane and heat is expected to spread out laterally through the film by conduction and convection. It is not easy to estimate these effects, but evidently an appreciable temperature increase can occur. Upon approaching the transition to a nematic or an isotropic phase this can lead to spontaneous thinning of the membrane.

The heat generated is sufficient to cause some convective instabilities inside the smectic membrane [44]. This results in fluctuations of the reflected intensity. Figure 5 shows changes of the rocking curve induced by removal of an attenuator of 25 μm Cu leading to 3 times more intensity. This increase of incident intensity results in a decrease of the scattered intensity. After inserting the attenuator back, the original rocking curve profile is restored after a few minutes. We attribute this behavior to hydrodynamic instabilities in the sample arising from convective flow caused by local density changes due to heating. This disturbs the orientation of the layer structure of the membrane, leading to a changing rocking curve as shown in Fig. 5. Evidently we are working at the limits of stability of the smectic membranes themselves. In the case of a 100-μm pinhole the heat load per unit volume is still the same, but the absolutely absorbed heat is two orders of magnitude larger. Hence variation of the pinhole can cause large changes in sample stability.

D. Neutron spin-echo setup

Neutron spin-echo measurements were performed at spectrometer IN15 of the Institut Laue-Langevin (ILL, Grenoble, France) [45]. Neutron contrast was obtained from 8CB with deuterated phenyl rings. Large-size membranes of 50×50 mm^2 were stretched on an aluminum frame to be illuminated by a neutron beam of about 40×10 mm^2. These membranes were not of uniform thickness; instead, several regions were observed with a thickness from about half a micron at the top of the vertical frame up to a few microns at the bottom. Wavelengths of 0.9 nm and 1.5 nm were selected, allowing time scales up to 40 ns and 100 ns, respectively. Scattered neutrons were registered by a 2D position-sensitive detector. Each point of the detector corresponds to a specific value of the projection $q_\perp$ of the scattering vector on the surface of the membrane (see Fig. 6). If $k=2\pi/\lambda$ is a wave vector of the neutron beam, we can write for the incident beam on the membrane

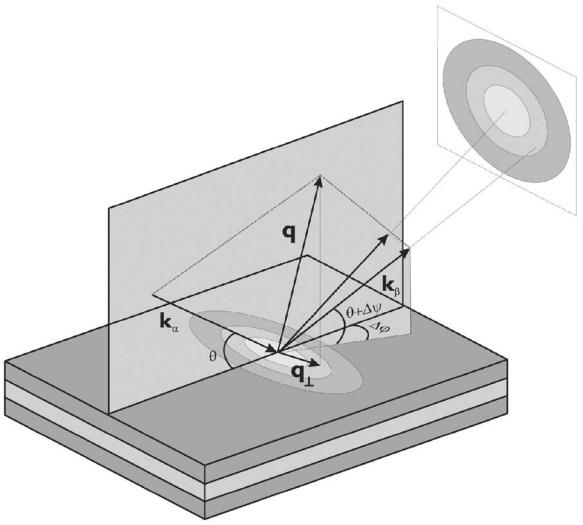

FIG. 6. Scattering geometry for NSE measurements of a smectic membrane in a reflection geometry.

$$q_x = k\cos\left(\frac{\vartheta_0}{2}+\omega\right), \tag{26}$$

$$q_y = 0, \tag{27}$$

$$q_z = k\sin\left(\frac{\vartheta_0}{2}+\omega\right). \tag{28}$$

For the outgoing beam we obtain

$$q_x = k\cos(\Delta\phi)\cos\left(\frac{\vartheta_0}{2}+\Delta\psi-\omega\right), \tag{29}$$

$$q_y = k\sin(\Delta\phi), \tag{30}$$

$$q_z = k\cos(\Delta\phi)\sin\left(\frac{\vartheta_0}{2}+\Delta\psi-\omega\right). \tag{31}$$

Summing up the components in q_x and q_y we arrive at the following expression for $q_\perp$ which corresponds to a point on the detector at angular displacement (δ,φ):

$$q_\perp = \frac{2\pi}{\lambda}\times\sqrt{[\cos(\Delta\varphi)\cos(\theta+\Delta\psi-\omega)-\cos(\theta+\omega)]^2+\sin^2(\Delta\varphi)}. \tag{32}$$

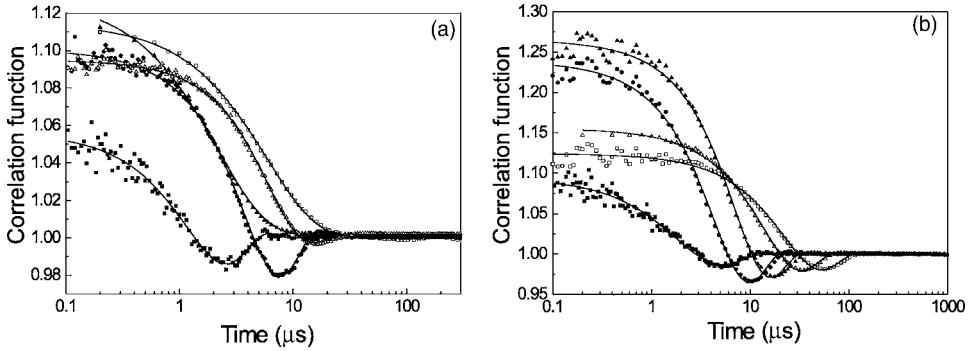

FIG. 7. Correlation functions from XPCS of smectic membranes of different thicknesses; lines indicate fits to Eq. (39). (a) 4O.8: Solid squares: 0.45 μm. Solid circles: 1.0 μm. Solid triangles: 2.2 μm. Open triangles: 6.0 μm. Open squares: 10.0 μm. (b) FPP: Solid squares: 0.48 μm. Solid circles: 2.8 μm. Solid triangles: 5.9 μm. Open triangles: 13.2 μm. Open squares: 15.0 μm.

To extract the $q_\perp$ dependence of the relaxation time we grouped points on the detector with close values of $q_\perp$. As the scattering directions with the same projection on the surface of the membrane form a cone, the corresponding points on the detector will form ellipses. Dividing the detector surface into three elliptic areas and integrating the contributions from all points in these regions, we constructed for each scattering angle three correlation functions.

In the NSE measurements, $S(q,t)$ was assumed to behave as a Kohlrausch-Williams-Watts (KWW) function [46,47]:

$$S(q,t) = \exp\left\{-\left(\frac{t}{\tau_{\mathrm{KWW}}}\right)^{\beta}\right\}. \tag{33}$$

This form arises from a broad superposition of exponentials with some distribution function $f(\tau)$ [48]:

$$\int_{-\infty}^{+\infty} f(\ln\tau)\exp\left(-\frac{t}{\tau}\right)d(\ln\tau) = \exp\left\{-\left(\frac{t}{\tau_{\mathrm{KWW}}}\right)^{\beta}\right\}. \tag{34}$$

In this case $S(q,t)$ can be written as

$$S(q,t) = \int_0^{\infty} d\tau f(\tau)\exp\left(-\frac{t}{\tau}\right). \tag{35}$$

From this equation, we can define the average value of τ as

$$\langle\tau\rangle = \int_0^{\infty} \tau f(\tau) d\tau. \tag{36}$$

Now we can calculate the following integral:

$$\int_0^{\infty} S(q,t)dt = \int_0^{\infty}\int_0^{\infty} dt d\tau f(\tau)\exp\left(-\frac{t}{\tau}\right) = \int_0^{\infty} d\tau f(\tau)\tau = \langle\tau\rangle.$$

On the other hand, we can use Eq. (35) and calculate the above integral exactly:

$$\int_0^{\infty} S(q,t)dt = \frac{\Gamma(1/\beta)}{\beta}\tau_{\mathrm{KWW}}. \tag{37}$$

Equating the results of the last two equations we conclude

$$\langle\tau\rangle = \frac{\Gamma(1/\beta)}{\beta}\tau_{\mathrm{KWW}}. \tag{38}$$

Fitting the NSE curves with a KWW exponential function and using Eq. (38), we obtained the average value of the relaxation time for each area section of the detector.

IV. EXPERIMENTAL RESULTS

Figure 7 shows typical intensity correlation functions from XPCS of smectic 4O.8 and FPP membranes of various thicknesses at the first-order specular Bragg position. The experimental curves were fitted to a simple oscillatory relaxation function:

$$\frac{\langle I(t)I(0)\rangle}{\langle I\rangle^2} = A\exp(-t/\tau)\cos(\omega t + \phi). \tag{39}$$

In thin membranes we note for both compounds an oscillatory behavior. In thicker membranes the oscillations shift to larger times, while for thick 4O.8 membranes the oscillations disappear completely and only exponential relaxation is left. In FPP membranes, at the first Bragg position the oscillatory relaxation is present for all thicknesses measured. The only exponential relaxation found in FPP membranes at any specular position was at the second Bragg peak (see Fig. 8).

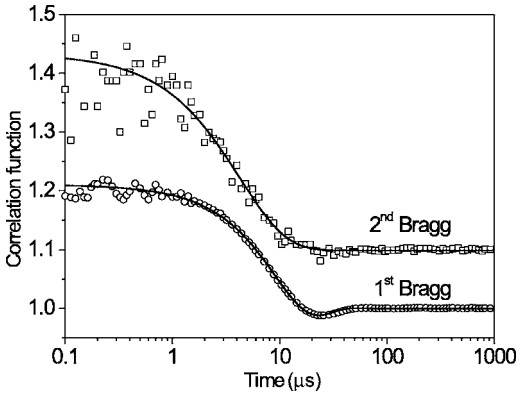

FIG. 8. Correlation functions measured at the first and second Bragg positions of a 13.2-μm-thick FPP membrane.

TABLE II. Fitting parameters for 4O.8 membranes.

Thickness (μm)	A	τ (μs)	ω (μs^{-1})	ϕ (rad)
0.037	0.06	2.0	0.86	0.40
0.068	0.04	3.9	0.32	0.52
0.3	0.03	5.9	0.29	0.41
1.0	0.10	5.4	0.33	0.08
2.2	0.13	2.2	0	0
5.0	0.05	9.7	0.14	−0.09
6.0	0.11	5.3	0.19	−0.48
10.0	0.11	5.9	0	0

TABLE III. Fitting parameters for FPP membranes.

Thickness (μm)	A	τ (μs)	ω (μs^{-1})	ϕ (rad)
0.047	0.15	2.8	0.25	0.88
0.64	0.15	11.4	0.05	0.95
2.8	0.24	5.8	0.24	0.17
3.0	0.24	2.6	0.28	0.02
5.9	0.27	8.2	0.15	−0.04
7.7	0.21	12.3	0.11	0.13
12.5	0.23	7.7	0.13	−0.49
13.2	0.16	18.7	0.07	0.20
15.0	0.13	31.7	0.04	0.33

The fitted values for the relaxation time τ and the frequency ω are given in Tables II and III, while their thickness dependence is plotted in Fig. 9. Even though the scatter of the experimental points is considerable, we can conclude that τ increases and ω decreases with membrane thickness. Note in Table II the anomalous behavior of a relatively thin 2.2-μm 4O.8 membrane that shows exponential relaxation, while both thinner and thicker membranes still display oscillatory behavior.

Figure 10(a) shows a series of off-specular measurements of 8CB membranes. Already for a small offset from the specular position corresponding to 10 mdeg, the oscillatory profile transforms into a pure exponential relaxation. The relaxation time remains about constant for all measured off-specular positions [see Fig. 10(b)]. Figure 11 illustrates the transition process from oscillatory to exponential relaxation in more detail for an FPP membrane. Close to the specular Bragg position oscillations are still detected; at slightly larger off-specular scattering angles the behavior changes into exponential relaxation.

On several occasions we obtained for highly ordered membranes a poor contrast for the correlation functions at the specular reflection position. This in spite of the fact that such samples with a narrow mosaic distribution show sharp and very intense specular reflections. This effect is illustrated in Fig. 12. At the center of the rocking curve hardly any contrast is left, which starts to develop as soon as we shift slightly (only 0.5 mdeg) off specular.

Figure 13(a) displays data obtained for 8CB membranes by NSE. At the specular position no relaxation is observed in this time range (below 50 ns) in agreement with the XPCS results of Fig. 10(a). The curves measured close to the specular position indicate a slow relaxation, while at the larger off-specular positions the relaxation time decreases [see Fig. 13(b)]. This behavior differs strongly from the approximately constant values of τ from XPCS at small off-specular angles shown in Fig. 10.

V. DISCUSSION

In the experimental part we have made empirical fits of the correlation functions to Eq. (39), which we shall interpret now in terms of the various contributions to the relaxation. We shall start the discussion with the relatively simple situation at large off-specular angles (which means larger than q_c). The wavelength of the determining largest fluctuation is set by the choice of the off-specular angle or equivalently $q_\perp$. In this region only exponential relaxation is observed. In the second part we consider smaller values of $q_\perp$ approaching $q_\perp \to 0$ and the effect of crossing q_c. As we shall see, in this regime two "external" effects need to be taken into account that influence the relaxation behavior. Around $q_\perp = 0$ the size of the coherence volume comes into play which prevents wavelength larger than this dimension to contribute to the relaxation. A second factor is the mosaic distribution of the sample, given by the width of the rocking curve. This width limits the range of projections of scattering vectors that contribute to the intensity at the Bragg position. The combination of these two effects determines a "window" of wavelength that can contribute to the relaxation.

A. Off-specular results: Surface and bulk-elastic regimes

In order to probe with XPCS fluctuations of a particular wavelength, the projection of the scattering vector on the

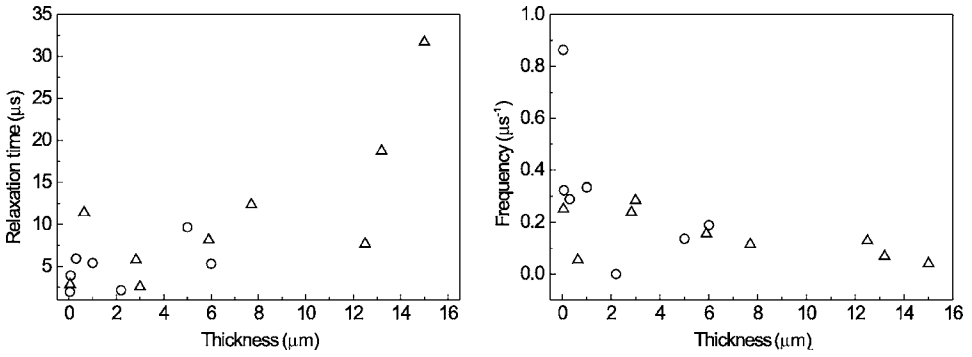

FIG. 9. Dependence of relaxation time and frequency of the oscillations on membranes thickness: Circles: 40.8. Triangles: FPP.

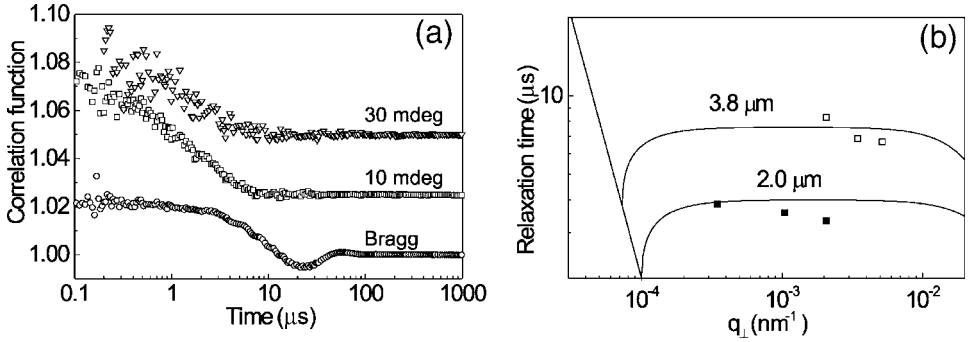

FIG. 10. XPCS measurements of 8CB membranes. (a) Correlation functions for a thickness of 2.0 μm at the off-specular scattering angles indicated. (b) Experimental relaxation times at off-specular positions for the thicknesses indicated; solid lines give the theoretically calculated dispersion curves.

membrane surface should match the wave vector of interest. In x-ray reflectivity this is accomplished by choosing an off-specular angle corresponding to the desired value of $q_\perp$. In Fig. 10(b) the relaxation times from such off-specular measurements are plotted together with the theoretical dispersion curves. In the range accessible by XPCS no dependence of the relaxation time on $q_\perp$ is observed, in agreement with the plateau in the theoretical dispersion curve. The relaxation times are determined by the surface tension and scale with the thickness of the membrane as expected from Eq. (24). Note that at these off-specular positions no reference signal is present, resulting in a homodyne detection scheme. According to the Siegert relation then the intensity correlation function is proportional to $|g_1(t)|^2$, which results for exponential decay in a relaxation time $\tau/2$. Hence the values obtained from the experiment have been multiplied by a factor 2 to obtain τ.

In XPCS the determination of the relatively fast relaxation times involved in smectic membranes requires a minimum intensity of the order of 10^4 cts/s. Hence, in spite of the large count rates at the specular Bragg position, the steep decrease of the scattered intensity with off-specular angle limits the accessible range of $q_\perp$ values. As a result, the accessible wave vector values are all at the plateau region of the dispersion curve. However, larger off-specular scattering angles could be achieved in NSE experiments. The large size of the neutron beam in combination with the integration over the detector area results in sufficiently large count rates at off-specular positions as large as several degrees. As the wavelength of the neutrons is comparable to the x-ray wavelength used, the offset angles in NSE of several degrees result in $q_\perp$-values up to two orders of magnitude larger than probed by XPCS.

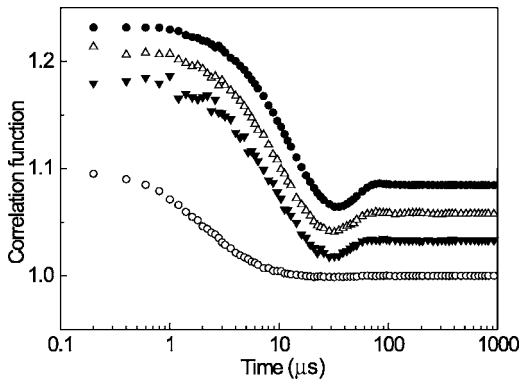

FIG. 11. Autocorrelation functions of a 13.2-μm-thick FPP membrane around the first Bragg position. Solid circles: specular position. Open triangles: 10-mdeg offset. Solid triangles: 12-mdeg offset. Open circles: 15-mdeg offset. The upper curves have been vertically shifted for clarity (from top to bottom) by 0.085, 0.06, and 0.03, respectively.

In Fig. 13(b) the averaged values of the NSE relaxation time [see Eq. (38)] are plotted together with the theoretical dispersion curves. These data show a $q_\perp$ dependence that can be related to bulk elastic effects. From Eq. (25) we expect a $1/q_\perp^2$ dependence of the relaxation time, well in agreement with the experimental results. Moreover, no thickness dependence is present anymore, as expected from theory, which is convenient in light of the nonuniform thickness of the large-size NSE samples. This leads to measurements that are a superposition of data for different values of L.

In the above discussions we assumed so far that the smectic membranes are incompressible. This approximation works well for fluctuations with a wave vector in the oscillatory or surface regime. It breaks down at larger $q_\perp$ values [10], for which a finite compressibility might play a role. As indicated in Fig. 13(b), the effect of a finite compressibility on the relaxation times manifests itself in a transition region between the surface and bulk-elasticity regimes. Some NSE results in Fig. 13(b) in the vicinity of this area extend above the high-compressibility limit, which could indicate that finite compressibility comes into play. However, these relaxation times in the range up to 100 ns are at the limit of the possibilities of NSE. Hence the correlation functions in this region carry significant uncertainty, which prevents any further quantitative analysis.

B. Specular results: Oscillating regime

It is clear that with decreasing off-specular angle we probe fluctuations with a smaller wave vector. Ultimately, at the specular position we reach the limit $q_\perp=0$. According to Fig. 2(a) in this limit the relaxation time should become infinite, while the experiments shown in Fig. 7 indicate finite times. Evidently, it is *a priori* not clear what is the decisive wave vector q_{mn} at the specular ridge. The experimental re-

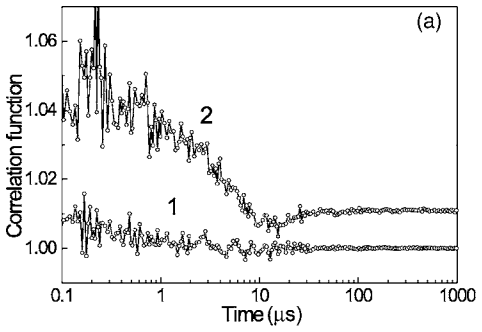

FIG. 12. XPCS measurements of a highly ordered (1-mdeg mosaic distribution) 0.05-μm-thick FPP membrane. (a) Correlation functions at the specular position $q_z=1.16$ nm^{-1} (1) and at half intensity (2). Curve 2 has been vertically shifted by 0.01 for clarity. (b) Rocking curve indicating the measurement positions.

sults suggest that also at the specular position some window of finite $q_\perp$ values determines the XPCS results by selecting fluctuations q_{mn} in the oscillatory regime. Accepting this assumption for a moment, let us investigate some of its implications. From Fig. 2(b) the frequency of the oscillations should become smaller for thicker membranes, which fits the observed shift of the minimum of the oscillations to slower times for thicker membranes in Fig. 7. For even thicker 4O.8 membranes the wave-vector window selects fluctuations from the exponential regime above the crossover wave vector q_c, leading to exponential relaxations at the specular ridge (Fig. 7). At the same membrane thickness, q_c is larger for FPP than for 4O.8. As q_c varies as $1/\sqrt{L}$ [see Eq. (20)], this causes for FPP potential exponential relaxations at the specular Bragg position to shift to larger thicknesses beyond our experimental possibilities. For FPP exponential relaxation at the specular ridge has only been observed at the second Bragg position. This indicates that the wave-vector window of contributing fluctuations has indeed shifted to larger values and passed q_c.

The above explanations evidently require that we can establish a window of $q_\perp$ values that defines the range of wave vectors q_{mn} dominating the XPCS measurements at the specular position. In the following we propose such a mechanism by a combination of two "filters," cutting the low- and high-wave-vector range, respectively. The high-pass "filter" is related to the movement of the illuminated area of the membrane as a whole (center-of-mass movement), the low-pass "filter" to the width of the rocking curve (mosaic distribution).

In Sec. II B we introduced the reference intensity signal I_0, which is related to the movement of the coherence volume as a whole. In other words to the movement of the center-of-mass (c.m.) of the coherence volume. Fluctuations of a wavelength larger than the size of the coherence volume contribute mainly to this c.m. movement. In contrast, fluctuations of a wavelength smaller than the coherence volume hardly shift the center of mass, but do contribute to the correlation function. Let us define $q_{\text{c.m.}}$ as the wave vector of a fluctuation of a wavelength matching the size of the coherence volume. The value of $q_{\text{c.m.}}$ is defined by the coherence properties of the incident beam and the resolution of the setup. To test this point of view, we make some rough estimates. The transverse coherence length of the incident beam is of the order of few microns; the projection on the membrane is about 100 μm. Using Eq. (20) we can predict for the different compounds the transition thickness for specular oscillating-exponential relaxation. For 40.8 this should occur at about 17 μm, which can be compared with the experimentally observed transition to the exponential regime close to 10 μm. For FPP a much larger value around 120 μm is predicted. As the thickest samples measured were $\lesssim$20 μm, this explains indeed why for FPP no transition to the exponential regime was observed at the specular Bragg position. On the other hand, at the second Bragg peak exponential relaxation was observed for a 13.2-μm FPP membrane (see Fig. 8). Because of the smaller projection of the coherence length at this position, the transition thickness would be about 30 μm. We conclude that the estimates given explain the data qualitatively rather well, but that quantitatively the predicted tran-

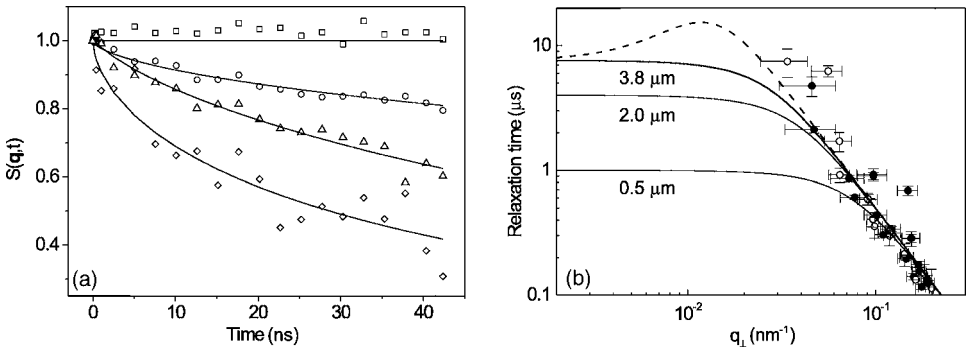

FIG. 13. NSE results of thick (μm range) 8CB membranes around the first Bragg position. (a) Intermediate scattering function for different positions: Squares: specular. Circles: 0.1-nm^{-1} offset. Triangles: 0.15-nm^{-1} offset. Diamonds: 0.24 nm^{-1}. Solid lines: fits to a KWW function with $\beta=0.59$. (b) Experimental relaxation times for various samples: open circles: NSE at 1.5 nm. Solid circles: NSE at 0.9 nm. Solid line: dispersion curves calculated for the thicknesses indicated (incompressible membranes). Dashed line: calculation for the 3.8 -μm membrane with finite compressibility ($B=10^6$ N/m^2).

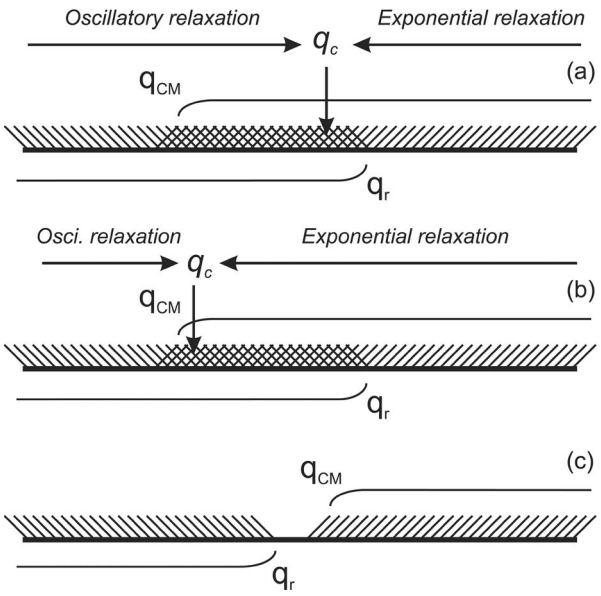

FIG. 14. Schematic representation of the window defined for XPCS by the center-of-mass movement and the mosaic distribution (see text). (a) The correlation function exhibits oscillatory relaxation when q_c is situated at the high-q side of the window. (b) As q_c shifts to lower q values in the window exponential relaxation takes over. (c) Representation of zero contrast near $q_\perp=0$.

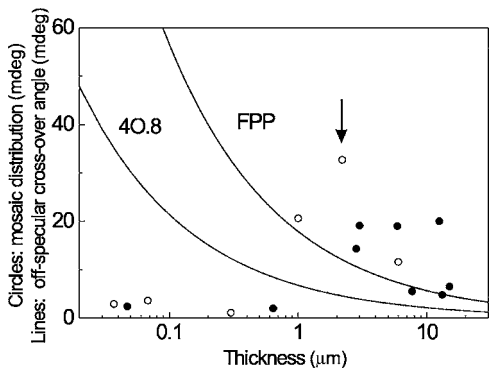

FIG. 15. Lines: thickness dependence of the scattering angle corresponding to q_c for 40.8 and FPP membranes. Circles: rocking curve widths for 40.8 (solid circles) and FPP (filled circles) for the thicknesses investigated. The arrow indicates exponential relaxation; all other points correspond to the oscillatory relaxation regime.

sition thicknesses are a factor of 2–3 larger than found experimentally. Obviously the agreement could be improved by reducing the estimated size of the coherence volume. In summary, $q_{\text{c.m.}}$ determines the edge of a wave-vector "high-pass filter." Only fluctuations of larger wave vector (smaller wavelength) contribute to the correlation function measured by XPCS. Shorter wave vectors (longer wavelengths) contribute mainly to the c.m. movement.

A second factor that influences the XPCS results is the mosaic distribution of the smectic membranes. It can be quantified using the width of the rocking curve, to be indicated as q_r. This width indicates a range of projections of scattering vectors that contribute to the intensity measured at the Bragg position. Each contribution corresponds to scattering from fluctuations with a wave vector matching the projection of the scattering vector on the surface of the membrane. The intensity profile of the rocking curve weights the contribution of each particular wave vector to the total intensity at the Bragg position. Hence q_r can be considered as a wave-vector "low-pass filter" of fluctuations influencing the XPCS signal, cutting off input from larger $q_\perp$ values. The contribution of each fluctuation is proportional to the intensity at the corresponding off-specular position. This will effectively suppress input from fluctuations with large values of q_{mn}.

Considering the three parameters $q_{\text{c.m.}}$, q_r, and q_c we can build a complete picture of the XPCS results. The quantities $q_{\text{c.m.}}$ and q_r define a window ("bandpass") determining the range of the wave vectors detected, which requires $q_r > q_{\text{c.m.}}$. In Figs. 14(a) and 14(b) we indicate two possible scenarios that depend crucially on the position of q_c with respect to this window. In case (a) the crossover wave vector q_c is positioned close to the upper edge of the window. In this situation mainly fluctuations *below* q_c contribute to the scattered intensity and we observe oscillatory behavior. In case (b) the positions of $q_{\text{c.m.}}$ and q_r are still the same, but q_c is situated closer to the lower edge of the window. Consequently, fluctuations *above* q_c will prevail and we expect simple exponential relaxation. The third case (c) differs from the previous ones in the absence of overlap between low- and high-pass filter ($q_r < q_{\text{c.m.}}$). This means that fluctuations contributing to the XPCS signal only translate the scattering volume as a whole without changing the total intensity. This results in the absence of the contrast in the corresponding specular measurements. This situation applies to the result at $q_\perp=0$ shown in Fig. 12.

Let us make some estimates to connect the experiments shown in Fig. 12 in more detail to the model of Fig. 14(c). At the specular position ($q_z=1.16\ \text{nm}^{-1}$) the width of rocking curves from the most uniform, resolution-limited samples is less than 1 mdeg. An offset of 1 mdeg corresponds to a projection of the scattering vector on the surface $q_x=2.0\times10^{-5}\ \text{nm}^{-1}$ or a lateral size of about 300 μm. This value is comparable to the estimated length of the coherence volume. Consequently, at the specular ridge fluctuations are detected with a wavelength larger than the coherence volume. As argued above, these do not contribute to the XPCS signal. On the other hand, contributions from shorter-wavelength fluctuations are not detected at the Bragg position because of the narrow rocking curve; they start to contribute only at off-specular positions. This is exactly the situation pictured in Fig. 14(c). As a result only membranes with a rocking curve width larger than about 1 mdeg provide enough contrast to measure a correlation function at the specular Bragg position. We conclude that the choice of our "window" of contributing wave vectors provides plausible explanations of the relatively complicated features observed in XPCS of smectic membranes.

There are two somewhat more detailed points worth discussing in the context of the general framework given above. Figure 15 displays the scattering angle corresponding to q_c

versus membrane thickness, separating regions of oscillatory and exponential relaxations. Superimposed are rocking curve widths from which position we can in principle estimate which regime applies. For points below the crossover curve the main contribution to the resulting XPCS signal stems from fluctuations with oscillatory relaxation. For the points well above the curves, fluctuations with exponential relaxations will play a major role. In Fig. 15 the arrow indicates a thin 2.2-μm 4O.8 membrane with accidentally an unusually large 32-mdeg broad mosaic distribution. This explains why we observe for this sample exponential relaxation, even through some thicker samples with narrower rocking curves still exhibit oscillatory behavior.

Finally, in Sec. II C we discussed the surface-dominated exponential relaxation regime for fluctuations with a wave vector $q_\perp > q_c$ leading to a relaxation time $\tau = \eta_3 L/(2\gamma)$. This result has been previously obtained in a quasistationary model neglecting inertia of the smectic membrane [22]. In such a model no oscillatory regime is present and the exponential relaxation regime extends to $q_\perp = 0$. A linear dependence of the relaxation time on thickness was reported by Price *et al.* [22] at the specular Bragg position for samples of various different materials with thicknesses $\gtrsim 5$ μm. Figure 15 indicates that for these thicknesses indeed exponential relaxations could be dominant. However, in these early XPCS measurements the mosaic distribution of the smectic membranes was rather large, about 50–100 mdeg, which might also play a role. Such large values of q_r lead in Fig. 14 to a broad overlap area; in particular the right edge of the window extends to large wave-vector values. This results in dominance of fluctuations with exponential relaxation, in agreement with the observation of exclusively exponential relaxation in the XPCS experiment of Ref. [22].

VI. CONCLUSIONS

Combining XPCS and NSE methods we have mapped out three different relaxation modes in smectic liquid crystal membranes: oscillatory relaxations, surface-dominated exponential relaxations, and bulk-elasticity-dominated exponential relaxations. A critical wave vector q_c separates the first from the latter regimes. Fluctuations with a wave vector $q_{mn} < q_c$ exhibit oscillatory relaxation while in the region $q_{mn} > q_c$ fluctuations lead to simple exponential relaxation. For small wave vectors q_{mn} (but above q_c) the exponential relaxation time does not depend on the wave vector and is defined by surface tension, thickness, and viscosity of the membrane. This behavior has been observed in a series of off-specular XPCS experiments, for which the relaxation time was independent of the scattering angle. For larger wave vectors q_{mn} the exponential relaxation times are determined by the bending elasticity of the smectic layers and decrease as $1/q_{mn}^2$. This regime has been probed by NSE measurements thanks to the accessibility of an order of magnitude larger off-specular scattering angles compared to XPCS. The results indicate a decrease of the relaxation time with increasing scattering angle as predicted.

XPCS measurement at specular positions are dominated by a "window" of wave vectors cutting longer and smaller values. This window results from a combination of the mosaic distribution of the smectic membranes (width of the rocking curve) selecting long-wavelength fluctuations and the size of the coherence volume, inside which only short-wavelength fluctuations perturb the density profile, and is given by the overlap of these two regimes. For thin membranes this window is dominated by fluctuations with $q_{mn} < q_c$, resulting in oscillatory behavior of the intensity correlation function. For thicker membranes the crossover wave vector q_c shifts towards smaller values and the window of contributing fluctuations is dominated by exponential relaxation. For extremely well-ordered membranes characterized by a narrow rocking curve $\lesssim 1$ mdeg, the wave-vector window is empty, which results in the absence of any contrast in the specular correlation function.

ACKNOWLEDGMENTS

We acknowledge the European Synchrotron Radiation Facility (ESRF) for providing the long-term beam time that made this work possible and Institut Laue-Langevin (ILL) for providing NSE measurement time. We express our gratitude to Anders Madsen and Igor Dolbnya for their important contribution to the XPCS experiments and to Bela Farago for the NSE measurements. This work is part of the research program of the "Stichting voor Fundamenteel Onderzoek der Materie" (FOM), which is financially supported by the "Nederlandse Organisatie voor Wetenschappelijk Onderzoek" (NWO).

APPENDIX A: EFFECTS OF THE FINITE-SIZE COHERENCE VOLUME

In this appendix we discuss the finite size of the coherence volume that can lead to a nonzero contribution of the term I_2 in Eq. (11). This has direct consequences for the validity of the Siegert relation. Let us denote the lateral size of the coherence volume as $2R$. Introducing Eq. (3) into the correlator of I_2, we can calculate the corresponding contribution to Eq. (4). We shall use new variables $\xi = \mathbf{r}_{1,\perp} + \mathbf{r}_{3,\perp}$ and $\eta = (\mathbf{r}_{1,\perp} - \mathbf{r}_{3,\perp})/2$. Introducing integration limits corresponding to the finite size and using that I_2 is a product of complex conjugate numbers, we obtain the following result:

$$
\begin{aligned}
I_2 &= \int\int\int\int d\mathbf{r}_1 d\mathbf{r}_3 d\mathbf{r}_2 d\mathbf{r}_4 e^{-i\mathbf{q}\cdot(\mathbf{r}_1+\mathbf{r}_3)} e^{i\mathbf{q}\cdot(\mathbf{r}_2+\mathbf{r}_4)} \\
&\quad \times \langle \Delta\rho(\mathbf{r}_1,0)\Delta\rho(\mathbf{r}_3,t)\rangle \langle \Delta\rho(\mathbf{r}_2,0)\Delta\rho(\mathbf{r}_4,t)\rangle \\
&= \left| \int_{-R}^{R} d\eta \int dz_1 dz_3 e^{-iq_z(z_1+z_3)} \langle \Delta\rho(\eta,z_1,0) \right. \\
&\quad \left. \times \Delta\rho(-\eta,z_2,t)\rangle \int_{-2(R-\eta)}^{2(R-\eta)} d\xi e^{-i\mathbf{q}_\perp \xi} \right|^2 \\
&= |\tilde{\rho}_{layer}(q_z)|^2 \left| 4\int_0^R d\eta \sum_{m,n=1}^{N} \exp\{-i(m+n)d\} \right. \\
&\quad \left. \times \langle e^{-iq_z[u(-\eta,0)+u(\eta,t)]} \rangle \frac{\sin[2q_\perp(R-\eta)]}{q_\perp R} R \right|^2 . \qquad \text{(A1)}
\end{aligned}
$$

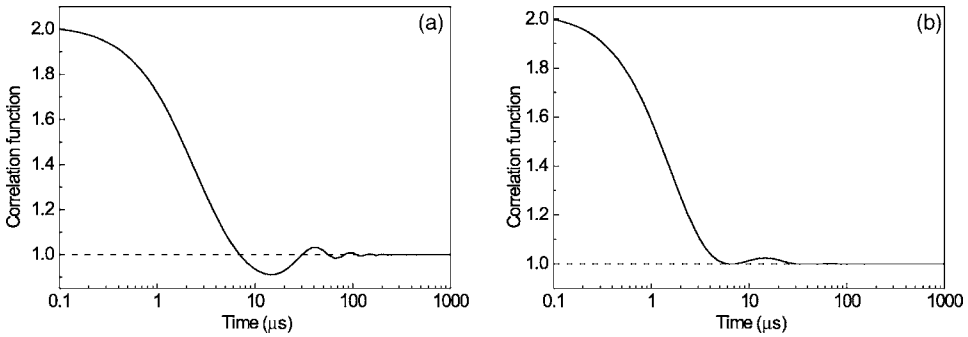

FIG. 16. Calculations of $g_2(\tau)$ for a 100-layer membrane: (a) without the term I_2 and (b) including I_2. The graphs are renormalized for clarity.

The term $\tilde{\rho}_{layer}(q_z)$ represents the Fourier transform of the density profile of a single smectic layer. For integration limits at infinity, this term would contribute a δ function to the scattering at the specular ridge ($\mathbf{q}_\perp=0$). For a finite-resolution setup, the δ-function contribution smears out and transforms into a function of the type $\sin(x)/x$ with a finite width in $\mathbf{q}_\perp$ space still centered at $\mathbf{q}_\perp=0$. Defining $g_+(\eta,t)=\langle[u(-\eta,0)+u(\eta,t)]^2\rangle$ and using $\langle\exp(ix)\rangle=\exp(-\langle x^2\rangle/2)$ we can rewrite I_2 in the form

$$I_2=|\tilde{\rho}_{layer}(q_z)|^2\left|4\int_0^R d\eta\exp\left(-\frac{q_z^2}{2}g_+(\eta,t)\right)\times\frac{\sin[2q_\perp(R-\eta)]}{q_\perp R}R\right|^2. \tag{A2}$$

In a similar way we can derive an expression for I_3. Defining new variables now as $\xi=\mathbf{r}_{1,\perp}+\mathbf{r}_{4,\perp}$, $\eta=(\mathbf{r}_{1,\perp}-\mathbf{r}_{4,\perp})/2$ and writing $g_-(\eta,t)=\langle[u(-\eta,0)-u(\eta,t)]^2\rangle$ we obtain

$$I_3=|\tilde{\rho}_{layer}(q_z)|^2\left|4\int_0^R d\eta\exp\left(-\frac{q_z^2}{2}g_-(\eta,t)\right)\times\cos(q_\perp R)(R-\eta)\right|^2. \tag{A3}$$

Using Eqs. (A2) and (A3) we can finally write $g_2(\tau)$ as

$$g_2(t)=1+\frac{\left|\int_0^R d\eta\exp\left(-\frac{q_z^2}{2}g_+(\eta,t)\right)\frac{\sin[2q_\perp(R-\eta)]}{q_\perp R}R\right|^2+\left|\int_0^R d\eta\exp\left(-\frac{q_z^2}{2}g_-(\eta,t)\right)\cos(q_\perp R)(R-\eta)\right|^2}{\left|\int_0^R d\eta\exp\left(-\frac{q_z^2}{2}g_-(\eta,0)\right)\cos(q_\perp R)(R-\eta)\right|^2}.$$

Figure 16 shows the effect of the contribution of I_2 to the calculation of the intensity correlation function for finite sizes. The curve in Fig. 16(b) indicates that the presence of I_2 shifts all oscillations above the baseline, creating a profile that cannot be obtained on the basis of the Siegert relation. Such oscillations have been observed in homodyne light scattering experiments of smectic membranes [49], which suggests that the term I_2 can be important for a correct treatment of scattering data in this regime.

APPENDIX B: LAYER DISPLACEMENT CORRELATION FUNCTION IN SMECTIC MEMBRANES

In this appendix we consider the theory of fluctuations in smectic membranes following Shalaginov and Sullivan [32]. These authors applied Fourier transforms both in space and time, solving the equation of motion in $(\mathbf{q},\omega)$ space. In the following treatment we avoid switching into ω space and solve the equation of motion in $(\mathbf{q},t)$ coordinates. We find such an approach more transparent, as in XPCS as well as in NSE experiments the energy of photons is not discriminated and the results are obtained in terms of the time-dependent intermediate scattering function $S(\mathbf{q},t)$.

Let us consider fluctuations of a rectangular smectic-A membrane of thickness L and lateral sizes (L_x,L_y). The free energy has the form of the Landau–de Gennes–Hołyst free energy [26,50]:

$$F=\frac{1}{2}\int d^2r_\perp\left\{\int_{-L/2}^{L/2}dz\{B[\nabla_z u(x,y,z)]^2\}+K[\nabla_\perp^2 u(x,y,z)]^2\}+\gamma\{[\nabla_\perp u(x,y,z=-L/2)]^2+[\nabla_\perp u(x,y,z=L/2)]^2\}\right\}. \tag{B1}$$

This functional form leads to the equation of motion

$$\rho_0 \frac{\partial^2 u(x,y)}{\partial t^2} = \eta_3 \frac{\partial}{\partial t} \nabla_\perp^2 u(x,y) + (B\nabla_z^2 - K\Delta_\perp^2) u(x,y), \quad \text{(B2)}$$

which must be completed with boundary conditions at the surfaces and edges of the membrane:

$$-\frac{\gamma}{B}\nabla_\perp^2 u(x,y,z = \pm L/2,t) \pm \nabla_z u(x,y,z = \pm L/2,t) = 0, \quad \text{(B3)}$$

$$u(0,y,z,t) = 0, u(L_x,y,z,t) = 0,$$

$$u(x,0,z,t) = 0, u(x,L_y,z,t) = 0. \quad \text{(B4)}$$

Because Eq. (B2) is a fourth-order equation in $r_\perp(x,y)$, two more boundary conditions are required at the lateral edges. These extra conditions will not have a much influence because the wavelengths of the fluctuations observed are orders of magnitude smaller than the size of the membrane. We have chosen the following two additional conditions, mainly because these are the only ones allowing to solve Eq. (B2) analytically:

$$u''(0,y,z,t) = 0, u''(L_x,y,z,t) = 0,$$

$$u''(x,0,z,t) = 0, u''(x,L_y,z,t) = 0. \quad \text{(B5)}$$

To analyze the scattering data the displacement-displacement time correlation function $g(\mathbf{r}_\perp,z,z',t) = \langle [u(0,z',0) - u(\mathbf{r}_\perp,z,t)]^2 \rangle$ must be computed. This correlation function can be expressed in the following form:

$$g(\mathbf{r}_\perp,z,z',t) = G(z,z) + G(z',z') - 2G(\mathbf{r}_\perp,z,z',t), \quad \text{(B6)}$$

$$G(z,z') = \langle u(0,z',0)u(0,z,0) \rangle, \quad \text{(B7)}$$

$$G(\mathbf{r}_\perp,z,z',t) = \langle u(0,z',0)u(\mathbf{r}_\perp,z,t) \rangle. \quad \text{(B8)}$$

In Eq. (B2) derivatives of $\mathbf{r}_\perp$ appear only as Laplace operators. Hence, we can expand the solution in a series of eigenfunctions of the Laplace operator that fulfill the boundary conditions, Eqs. (B5) and (B6):

$$u(x,y,\theta,z,t) = \sum_{m,n=0}^{\infty} A_{mn}(z,t) \sin\left(\frac{\pi m}{L_x}x\right) \sin\left(\frac{\pi n}{L_y}y\right). \quad \text{(B9)}$$

From this equation we obtain the correlation function $G(\mathbf{r}_\perp,z,z',t)$ in the following form:

$$G(\mathbf{r}_\perp,z,z',t) = \int_0^{L_x}\int_0^{L_y} dxdy \sum_{m,n}\sum_{k,p} A_{mn}(z,t)A_{kp}(z',t) \times \sin\left(\frac{\pi m}{L_x}x\right)\sin\left(\frac{\pi n}{L_y}y\right) \times \sin\left(\frac{\pi k}{L_x}(x+x')\right)\sin\left(\frac{\pi p}{L_y}(y+y')\right)$$

$$= \sum_{m,n} G_{mn}(z,z',t)\cos\left(\frac{\pi m}{L_x}x'\right)\cos\left(\frac{\pi n}{L_y}y'\right). \quad \text{(B10)}$$

An equation similar to Eq. (B2) holds for the corresponding Fourier amplitudes $G_{mn}(z,z',t)$ [32]:

$$\rho_0 \frac{\partial^2 G_{mn}(z,z',t)}{\partial t^2} = -\eta_3 q_{mn}^2 \frac{\partial}{\partial t} G_{mn}(z,z',t) + (B\nabla_z^2 - Kq_{mn}^4) G_{mn}(z,z',t), \quad \text{(B11)}$$

in which

$$q_{mn}^2 = \left(\frac{\pi m}{L_x}\right)^2 + \left(\frac{\pi n}{L_y}\right)^2. \quad \text{(B12)}$$

$G_{mn}(z,z',t)$ fulfills following the following initial and boundary conditions:

$$G_{mn}(z,z',0) = G_{mn}^0(z,z'), \quad \text{(B13)}$$

$$\frac{\gamma q_{mn}^2}{B} G_{mn}(z = \pm L/2,z',t) \pm \nabla_z G_{mn}(z = \pm L/2,z',t) = 0, \quad \text{(B14)}$$

Here $G_{mn}^0(z,z')$ is the Fourier amplitude of the equilibrium correlation function corresponding to the wave vector q_{mn} calculated in Ref. [27]. In order to solve Eq. (B11) we separate the variables t and z:

$$\frac{\partial^2 G_{mn}(z,z',0)}{\partial^2 z} + \frac{\lambda}{B} G_{mn}(z,z',0) = 0, \quad \text{(B15)}$$

$$\rho_0 \frac{\partial^2 G_{mn}(z,z',t)}{\partial t^2} + \eta_3 q_{mn}^2 \frac{\partial}{\partial t} G_{mn}(z,z',t) + (Kq_{mn}^4 + \lambda) G_{mn}(z,z',t) = 0, \quad \text{(B16)}$$

The solution can be represented in the form

$$G_{mn}(z,z',t) = A(\lambda,t)\sin\left(\sqrt{\frac{\lambda}{B}}z\right) + B(\lambda,t)\cos\left(\sqrt{\frac{\lambda}{B}}z\right). \quad \text{(B17)}$$

In order to fulfill the boundary conditions at the top and bottom surfaces of the film we need the roots of the following equations:

$$\cot\left(\lambda_i \frac{L}{2}\right) = -\frac{\gamma q_{mn}^2}{\lambda_i B}, \quad \text{(B18)}$$

$$\tan\left(\mu_i \frac{L}{2}\right) = \frac{\gamma q_{mn}^2}{\mu_i B}. \quad \text{(B19)}$$

From these equations we get an infinite spectrum of solutions $\{\lambda_i, \mu_i\}$. Now $G_{mn}(z,z',t)$ can be represented in the form

$$G_{mn}(z,z',t) = \sum_{i=0}^{\infty} A(\lambda_i,t)\sin(\lambda_i z) + B(\mu_i,t)\cos(\mu_i z), \tag{B20}$$

where $A(\lambda_i,t)$ and $B(\mu_i,t)$ are solutions of Eq. (B16). They can be written as

$$A(\lambda_i,t) = S_1(\lambda_i)\exp\left(-\frac{t}{\tau_1}\right) + S_2(\lambda_i)\exp\left(-\frac{t}{\tau_2}\right), \tag{B21}$$

$$B(\mu_i,t) = C_1(\mu_i)\exp\left(-\frac{t}{\tau_1}\right) + C_2(\mu_i)\exp\left(-\frac{t}{\tau_2}\right). \tag{B22}$$

Applying the initial conditions we find

$$A(\lambda_i,t) = \frac{G^s(\lambda_i,z')}{\tau_{s,1}-\tau_{s,2}}\left[\tau_{s,1}\exp\left(-\frac{t}{\tau_{s,1}}\right) - \tau_{s,2}\exp\left(-\frac{t}{\tau_{s,2}}\right)\right], \tag{B23}$$

$$B(\mu_i,t) = \frac{G^c(\mu_i,z')}{\tau_{c,1}-\tau_{c,2}}\left[\tau_{c,1}\exp\left(-\frac{t}{\tau_{c,1}}\right) - \tau_{c,2}\exp\left(-\frac{t}{\tau_{c,2}}\right)\right], \tag{B24}$$

where

$$G^s(\lambda_i,z') = \frac{2}{L}\int_{-L/2}^{L/2} G^0_{mn}(z,z')\sin(\lambda_i z)dz, \tag{B25}$$

$$G^c(\mu_i,z') = \frac{2}{L}\int_{-L/2}^{L/2} G^0_{mn}(z,z')\cos(\mu_i z)dz. \tag{B26}$$

Using the expression for $G^0_{mn}(z,z')$ given in Ref. [27] and using the boundary conditions from Eqs. (B18) and (B19) we can find exact analytical forms for the above integrals:

$$G^s(\lambda_i,z') = \frac{2k_BT}{BL(g^2+\lambda_i^2)}\left\{\sin(\lambda_i z') + \frac{2a^2\left[g\cosh\left(\frac{gL}{2}\right) + a\sinh\left(\frac{gL}{2}\right)\right]}{g\Delta}\sin\left(\frac{\lambda_i L}{2}\right)\sinh(gz')\right\}, \tag{B27}$$

$$G^c(\mu_i,z') = \frac{2k_BT}{BL(g^2+\mu_i^2)}\left\{\cos(\mu_i z') + \frac{2a^2\left[g\sinh\left(\frac{gL}{2}\right) + a\cosh\left(\frac{gL}{2}\right)\right]}{g\Delta}\cos\left(\frac{\mu_i L}{2}\right)\cosh(gz')\right\}, \tag{B28}$$

where $g=q_{mn}^2\sqrt{K/B}$, $a=\gamma q_{mn}^2/B$, and $\Delta=(g^2+a^2)\cosh(gL)+2ga\sinh(gL)$. The times $\tau_{s,(1,2)}$ and $\tau_{c,(1,2)}$ depend on the parameters $\{\lambda_i,\mu_i\}$ and can be found from the following relations:

$$\tau_{s,(1,2)}(\lambda_i) = \frac{2\rho}{\eta_3 q_{mn}^2}\left(1 \pm \sqrt{1-\frac{4\rho}{\eta_3^2 q_{mn}^4}(Kq_{mn}^4 + B\lambda_i^2)}\right)^{-1}, \tag{B29}$$

$$\tau_{c,(1,2)}(\mu_i) = \frac{2\rho}{\eta_3 q_{mn}^2}\left(1 \pm \sqrt{1-\frac{4\rho}{\eta_3^2 q_{mn}^4}(Kq_{mn}^4 + B\mu_i^2)}\right)^{-1}. \tag{B30}$$

Summarizing the above calculations we can write the real-space correlation function in the following form:

$$G(x,y,z,z',t) = \sum_{m,n=1}^{\infty}\cos\left(\frac{\pi m}{L_x}x\right)\cos\left(\frac{\pi n}{L_y}y\right)\left\{\sum_{i=0}^{\infty}\frac{\tau_{c,1}\exp\left(-\frac{t}{\tau_{c,1}}\right) - \tau_{c,2}\exp\left(-\frac{t}{\tau_{c,2}}\right)}{\tau_{c,1}-\tau_{c,2}}G_i^c(\mu_i,z')\cos(\mu_i z)\right.$$
$$\left. + \frac{\tau_{s,1}\exp\left(-\frac{t}{\tau_{s,1}}\right) - \tau_{s,2}\exp\left(-\frac{t}{\tau_{s,2}}\right)}{\tau_{s,1}-\tau_{s,2}}G_i^s(\lambda_i,z')\sin(\mu_i z)\right\}. \tag{B31}$$

From Eqs. (B27) and (B28) we note that $G_i^s(\lambda_i,z')$ and $G_i^c(\mu_i,z')$ decrease for increasing values of the undulation wave vector q_{mn} and the compression wave vectors $\{\lambda_i,\mu_i\}$. This means that Eq. (B31) is dominated by the fluctuations with the smallest wave vector (largest wavelength).

Let us consider the high-compressibility limit for which $B\to\infty$. In this case, we can find analytical solutions for Eqs. (B18) and (B19). As the dominant modes are the ones with the smallest wave vector, we consider only the smallest root μ_1. Approximating the tangent in Eq. (B19) by a linear function we obtain

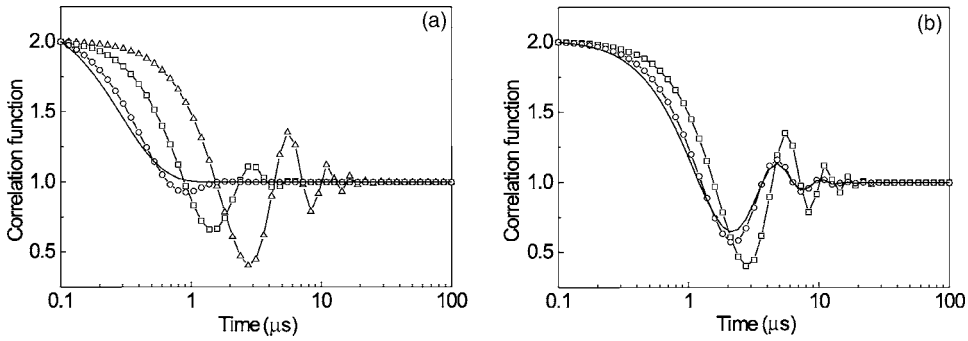

FIG. 17. Calculated correlation functions for a 10-mm-long and 0.5-μm-thick FPP membrane. (a) Single fluctuations with wave vector number m as follows: Triangles: 500. Squares: 1000. Circles: 2000. Solid line: 3000. (b) Dependence of the correlation function on the upper limit of the sum in Eq. (B34) for the lower limit set at 500. Upper limits as follows: Squares: 501. Circles: 1000. Solid line: 2000. The graphs are renormalized for clarity.

$$\mu_1 = \sqrt{\frac{2\gamma}{LB}} q_{mn}. \tag{B32}$$

Using this value for μ_1 we find for $G_1^c(q_{mn}, z')$ the following expression:

$$G_1^c(q_{mn}) = \frac{2k_BT}{KLq_{mn}^4 + 2\gamma q_{mn}^2}. \tag{B33}$$

Equation (B31) now reduces to the form

$$G(x,y,t) = 2k_BT \sum_{m,n=1}^{\infty} \frac{1}{KLq_{mn}^4 + 2\gamma q_{mn}^2} \cos\left(\frac{\pi m}{L_x} x\right) \times \cos\left(\frac{\pi n}{L_y} y\right) \frac{\tau_1 \exp\left(-\frac{t}{\tau_1}\right) - \tau_2 \exp\left(-\frac{t}{\tau_2}\right)}{\tau_1 - \tau_2}. \tag{B34}$$

Introducing μ_1 into Eqs. (B30) and (B29) the relaxation times τ_1 and τ_2 are

$$\frac{1}{\tau_{1,2}} = \frac{\eta_3 q_{mn}^2}{2\rho_0}\left[1 \mp i\sqrt{\frac{4\rho_0}{\eta_3^2 q_{mn}^4}\left(Kq_{mn}^4 + \frac{2\gamma}{L} q_{mn}^2\right) - 1}\right] = a(q_{mn}) \mp if(q_{mn}), \tag{B35}$$

which was introduced as Eq. (16) in Sec. II C.

Equation (B34) indicates that the layer-displacement correlation function depends on a superposition of contributions of fluctuations with different wave vectors. By changing the limits of the summation we can investigate which wave vectors contribute most to the correlation function. For the sake of simplicity we consider for this exercise a one-dimensional case, omitting the y dependence in the correlator $G(x,y,t)$. Now the summation in Eq. (B34) is performed over one index only and the wave vector is defined as $q_m = (\pi m / L_x)$. Figure 17(a) shows the result of a series of calculations of the intensity correlation function in which the correlator $G(x,t)$ is defined by a single fluctuation. This is achieved by taking only one term in Eq. (B34) with index m corresponding to the chosen wave vector. We observe that for higher-order fluctuations the oscillations are weaker. At a crossover point $m=3000$ all oscillations disappear. Figure 17(b) displays the cumulative effect of the fluctuations on the intensity correlation function. Fixing the lower limit of the summation in $G(x,t)$ at $m=500$ and extending the summation to larger values of m, we see that, compared to Fig. 17(a), the oscillations hardly change. This behavior indicates that the resulting correlation function is mainly defined by the interval of the shortest wave vectors included in Eq. (B34). This argument has been used in Sec. V B as a basis for the introduction of a "window" of wave vectors dominating the correlation functions as measured in XPCS.

[1] W. H. de Jeu, B. I. Ostrovskii, and A. N. Shalaginov, Rev. Mod. Phys. **75**, 181 (2003), and references therein.
[2] A. Caillé, C. R. Seances Acad. Sci., Ser. B **274**, 891 (1972).
[3] J. Als-Nielsen, J. D. Litster, R. J. Birgeneau, M. Kaplan, C. R. Safinya, A. Lindegaard-Andersen, and S. Mathiesen, Phys. Rev. B **22**, 312 (1980).
[4] C. R. Safinya, D. Roux, G. S. Smith, S. K. Sinha, P. Dimon, N. A. Clark, and A. M. Bellocq, Phys. Rev. Lett. **57**, 2718 (1986).
[5] See, for example, P. M. Chaikin and T. C. Lubensky, *Principles of Condensed Matter Physics* (Cambridge University Press, Cambridge, England, 1995).
[6] G. Friedel, Ann. Phys. (Paris) **18**, 273 (1922).
[7] C. Y. Young, R. Pindak, N. A. Clark, and R. B. Meyer, Phys. Rev. Lett. **40**, 773 (1978).
[8] C. Rosenblatt, R. Pindak, N. A. Clark, and R. B. Meyer, Phys. Rev. Lett. **42**, 1220 (1979).
[9] D. E. Moncton and R. Pindak, Phys. Rev. Lett. **43**, 701 (1979).
[10] E. A. L. Mol, J. D. Shindler, A. N. Shalaginov, and W. H. de Jeu, Phys. Rev. E **54**, 536 (1996).
[11] E. A. L. Mol, G. C. L. Wong, J. M. Petit, F. Rieutord, and W. H. de Jeu, Phys. Rev. Lett. **79**, 3439 (1997).
[12] B. Chu, *Laser Light Scattering: Basic Principles and Practice*

(Academic Press, San Diego, 1991).
[13] S. Dierker, NSLS Newslett. 2 (1995).
[14] G. Grübel and D. L. Abernathy, Proc. SPIE **3154**, 103 (1997).
[15] D. L. Abernathy, G. Grübel, S. Brauer, I. McNulty, G. B. Stephenson, S. G. J. Mochrie, A. R. Sandy, N. Mulders, and N. Sutton, J. Synchrotron Radiat. **5**, 37 (1998).
[16] A. Böttger and J. G. H. Joosten, Europhys. Lett. **4**, 1297 (1987).
[17] F. Nallet, D. Roux, and J. Prost, J. Phys. (Paris) **50**, 3147 (1989).
[18] S. G. J. Mochrie, L. B. Lurio, A. Ruhm, D. Lumma, M. Borthwick, P. Falus, H. J. Kim, J. K. Basu, J. L. J., and S. K. Sinha, Physica B **336**, 173 (2003).
[19] A. Madsen, B. Struth, and G. Grübel, Physica B **336**, 216 (2003).
[20] A. Madsen, T. Seydel, M. Sprung, C. Gutt, M. Tolan, and G. Grübel, Phys. Rev. Lett. **92**, 096104 (2004).
[21] H. Y. Kim, A. Ruhm, L. B. Lurio, J. K. Basu, J. Lal, S. G. J. Mochrie, and S. K. Sinha, Mater. Sci. Eng., C **24**, 11 (2004).
[22] A. C. Price, L. B. Sorensen, S. D. Kevan, J. Toner, A. Poniewierski, and R. Hołyst, Phys. Rev. Lett. **82**, 755 (1999).
[23] A. Fera, I. P. Dolbnya, G. Grübel, H. G. Muller, B. I. Ostrovskii, A. N. Shalaginov, and W. H. de Jeu, Phys. Rev. Lett. **85**, 2316 (2000).
[24] I. Sikharulidze, I. P. Dolbnya, A. Fera, A. Madsen, B. I. Ostrovskii, and W. H. de Jeu, Phys. Rev. Lett. **88**, 115503 (2002).
[25] I. Sikharulidze, B. Farago, I. P. Dolbnya, A. Madsen, and W. H. de Jeu, Phys. Rev. Lett. **91**, 165504 (2003).
[26] R. Hołyst, Phys. Rev. A **44**, 3692 (1991).
[27] A. N. Shalaginov and V. P. Romanov, Phys. Rev. E **48**, 1073 (1993).
[28] A. Yu. Val'kov, V. P. Romanov, and A. N. Shalaginov, Phys. Usp. **37**, 139 (1994).
[29] A. Poniewierski, R. Hołyst, A. C. Price, L. B. Sorensen, S. D. Kevan, and J. Toner, Phys. Rev. E **58**, 2027 (1998).
[30] H.-Y. Chen and D. Jasnow, Phys. Rev. E **61**, 493 (2000).
[31] L. V. Mirantsev, Phys. Rev. E **62**, 647 (2000).
[32] A. N. Shalaginov and D. E. Sullivan, Phys. Rev. E **62**, 699 (2000).
[33] V. P. Romanov and S. V. Ul'yanov, Phys. Rev. E **63**, 031706 (2001).
[34] V. P. Romanov and S. V. Ul'yanov, Phys. Rev. E **65**, 021706 (2002).
[35] S. Mora and J. Daillant, Eur. Phys. J. B **27**, 417 (2002).
[36] V. P. Romanov and S. V. Ul'yanov, Phys. Usp. **46**, 915 (2003).
[37] S. Sprunt, M. S. Spector, and J. D. Litster, Phys. Rev. A **45**, 7355 (1992).
[38] I. Sikharulidze, I. P. Dolbnya, A. Madsen, and W. H. de Jeu, Opt. Commun. **247**, 111 (2005).
[39] J. C. Earnshaw, Appl. Opt. **36**, 7583 (1997).
[40] C. D. Cantrell, Phys. Rev. A **1**, 672 (1970).
[41] C. Rosenblatt and N. Amer, Appl. Phys. Lett. **36**, 432 (1980).
[42] P. Pieranski *et al.*, Physica A **194**, 364 (1993).
[43] A. Q. R. Baron, Hyperfine Interact. **125**, 29 (2000).
[44] A. Zywocinski, F. Picano, P. Oswald, and J. C. Géminard, Phys. Rev. E **62**, 8133 (2000).
[45] B. Farago, Physica B **268**, 270 (1999).
[46] F. Kohlrausch, Pogg. Ann. Phys. **119**, 352 (1863).
[47] G. Williams and D. C. Watts, Trans. Faraday Soc. **66**, 80 (1970).
[48] A. Arbe, J. Colmenero, M. Monkenbusch, and D. Richter, Phys. Rev. Lett. **81**, 590 (1998).
[49] W. H. de Jeu, A. Madsen, I. Sikharulidze, and S. Sprunt, Physica B **357**, 39 (2005).
[50] P. G. de Gennes and J. Prost, *The Physics of Liquid Crystals* (Clarendon Press, Oxford, 1993).